ARTICLE   OPEN

Check for updates

Unveiling nano-scaled chemical inhomogeneity impacts on corrosion of Ce-modified 2507 super-duplex stainless steels

Harishchandra Singh [1], Yi Xiong[2,3 ✉], Ekta Rani[1], Shubo Wang [1], Mourad Kharbach[1], Tian Zhou[2], Huai Yao[2,3], Yuran Niu[4], Alexei Zakharov[4], Graham King [5], Frank M. F. de Groot[6], Jukka Kömi[7], Marko Huttula[1,2] and Wei Cao [1 ✉]

The widely used stainless steels and their deformed variants are anticorrosive in ambient conditions due to passivation layers composed of chromium oxides. Conventionally, corrosion and erosion of the steels are attributed to the breakdown of such layers but seldomly to the origin that depends on surface heterogeneity at the microscopic level. In this work, the nanometer-scaled chemical heterogeneity at the surface unveiled via spectro-microscopy and chemometric analysis unexpectedly dominates the breakdown and corrosion behavior of the cold-rolled Ce-modified 2507 super-duplex stainless steels (SDSS) over its hot-deformed counterpart. Though relatively uniformly covered by a native Cr_2O_3 layer revealed by X-ray photoemission electron microscopy, the cold-rolled SDSS behaved poorly in passivity because of locally distributed Fe^{3+} rich nano-islands over the Fe/Cr oxide layer. This atomic-level knowledge provides a deep understanding of corrosion of stainless steel and is expected to benefit corrosion controls of similar high-alloyed metals.

INTRODUCTION

Since the invention of stainless steel, anticorrosive properties of the chromium-iron alloy have been attributed to chromium which forms a strong oxide/oxyhydroxide that renders passive behavior in most environments. Super duplex stainless steels (SDSS) with better corrosion resistance are endowed with superior mechanical properties over conventional (austenitic and ferritic) stainless steels[1–3]. The enhanced mechanical strength enables lighter and more compact designs. In contrast, the high pitting and crevice corrosion resistance of cost-effective SDSS ensures longer life-times, extending their applications to pollution control, chemical vessels, and the offshore oil/gas industries[4]. However, the narrow hot working temperature range and poor forming properties hinder its practical applications at a large scale[5]. Thus, the SDSS is modified to enhance the aforesaid performances. For example, the Ce-modification was introduced to the 2507 SDSS (Ce-2507) along with a high N addition[6–8]. The rare-earth element (Ce) at a suitable concentration of 0.08 wt% is beneficial to the mechanical proper-ties of DSS because of enhanced grain refinements and grain boundary strengths. Wear and corrosion resistance, tensile and yield strength, and hot workability were also improved[9]. The larger amount of N can substitute the expensive Ni content, making the SDSS more cost-effective[10].

Recently, the SDSS was plastically deformed at different temperatures (cryogenic, cold, and hot) to reach superior mechanical performances[6–8]. However, the superior corrosion resistance of SDSS, resulting from the presence of a thin oxide film on the surface, is subjected to many factors, e.g., intrinsic heterogeneous microstructures resulting from the presence of multiple phases with different grain boundaries, unwanted precipitates and different responses of varied austenite and ferrite phases to deformations[7]. Thus, investigations of microregional

properties of such thin films down to electronic structure levels become crucial to understand corrosion of the SDSS and require sophisticated experimental techniques. So far, surface-sensitive methods such as Auger electron spectroscopy[11] and X-ray photoelectron spectroscopy[12–15], and hard X-ray photoelectron emission microscopy (HAX-PEEM)[16], while providing chemical distinctions of surface layers, typically fail to separate the chemical state of the same element at spatially different positions at the nanoscale. Few recent studies correlated the local chromium oxidation to the observed corrosion behaviors on austenitic stainless steel[17], martensitic steel[18], and SDSS[19,20]. However, these studies focused mainly on the heterogeneity in Cr (for example, Cr^{3+} oxidation state) on the corrosion resistance. Lateral hetero-geneity in the oxidation state of the element can result from different compounds with identical composition elements, e.g., iron oxides. These compounds inherit refined sizes subjected to thermomechanical treatments, tightly adjacent to each other but vary in compositions and oxidation states[16,21]. Thus, unveiling the breakdown of oxide film and then pitting corrosion demands knowledge of surface heterogeneity at microscopic level. Despite the demands, a quantitative assessment, such as on lateral heterogeneity in the oxidation especially of Fe at nano-/atomic-scale, is still missing and its correlation with the corrosion resistance remains unexplored. Only recently, the chemical state of various elements, such as Fe and Ca has been quantitatively described on steel samples by soft X-ray photoemission electron microscopy (X-PEEM) at synchrotron radiation facilities at the nanoscale[22]. Combined with the chemically sensitive X-ray absorption spectroscopy (XAS) method, X-PEEM, involving mea-surement of XAS with the high spatial and spectral resolution, provides chemical information regarding the elemental composi-tion and its chemical state within a spatial resolution down to the
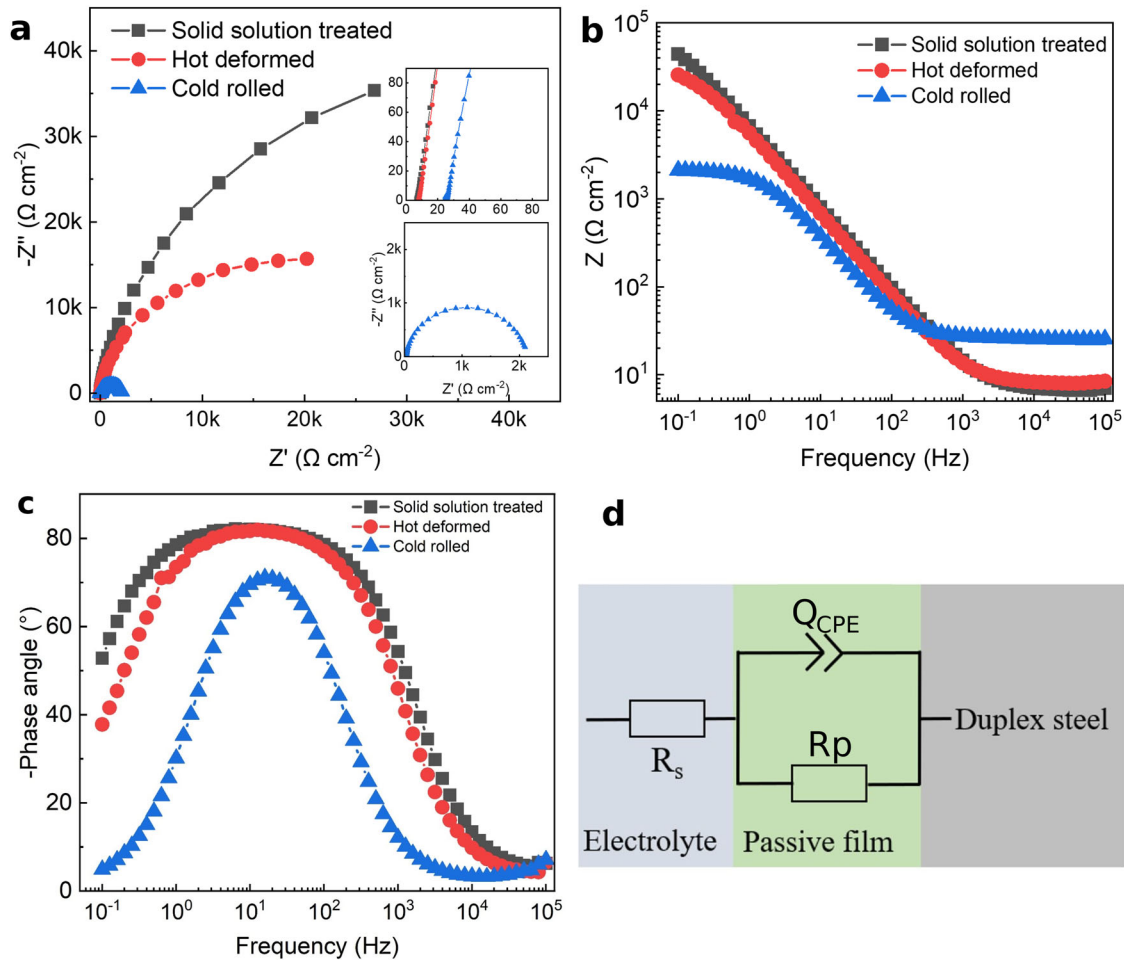
Fig. 1 Electrochemical impedance spectroscopy (EIS) measurements of the selected SDSS samples in acidic (pH = 1) FeCl$_3$ solution at room temperature. a Nyquist, **b**, **c** Bode impedance and phase plots, and **d** corresponding equivalent electrical circuit model, where R_S is the electrolyte resistance, R_p is the polarization resistance and Q_{CPE} is a constant phase element for modeling the non-ideal capacitance (n) of the oxide layer. The EIS measurements were carried out at open circuit potential.

nanometer scale[23]. Such a spectro-microscopic insight into the initiation sites benefits local chemical probation and may evidence chemical variations in Fe layers spatially that have not been explored before.

The present study advances PEEM's merits in detecting chemical distinctions at the nanoscale and brings in an insightful surface analysis approach at the atomic level to understand the corrosion behavior of Ce-2507. It employs the K-means clustering chemometrics methods[24] to plot global chemical (in)homogeneities of involved elements whose chemical states are presented in a statistical representation. Unlike corrosion triggered by chromium oxide film breakdown in conventional cases, the present poor passivity then low corrosion resistance is attributed to the localized Fe^{3+} rich nano-islands against the vicinity over the Fe/Cr oxide layer which could be the breakdown sites of the protective oxide film and lead to corrosion.

RESULTS AND DISCUSSION
Corrosion behavior
The corrosion behavior of deformed 2507 SDSS was first assessed through electrochemical measurements. Figure 1 depicts the Nyquist and Bode curves for the selected samples in acidic (pH = 1) FeCl$_3$ aqueous solution at room temperature. The chosen electrolyte serves as a strong oxidizing agent to characterize the passive film's breakdown propensity. Although the material did

Table 1. Fit results, including R_S, R_p, Q_{CPE}, and n, of the EIS equivalent circuit model (Fig. 1d) for SDSS samples.

Materials	R_s (Ω cm^{-2})	R_p (kΩ cm^{-2})	Q_{CPE} (s^n Ω^{-1} cm^{-2})	n
Solid solution	6.99	135	31.0	0.929
Hot deformed	8.06	34.7	32.9	0.918
Cold rolled	25.60	2.1	57.6	0.920

not undergo stable pitting corrosion at room temperature, the analyses provide insights into understanding potential breakdown events and following corrosion. The equivalent electrical circuit (Fig. 1d) was employed to fit the electrochemical impedance spectroscopy (EIS) spectra, and the corresponding fitting results are given in Table 1. Incomplete semicircles turned out in tests of solid solution treated and hot-deformed samples, while a compressed semicircle (Fig. 1b) in cold-rolled counterpart. In EIS spectra, the radius of the semicircle can be regarded as the polarization resistance (R_p)[25,26]. The R_p of the solid solution treated SDSS in Table 1 is about 135 kΩ cm^{-2}; nevertheless, a much lower value of 34.7 and 2.1 kΩ cm^{-2} for hot-deformed and cold-rolled SDSS, respectively, is seen. This significant decline in R_p displays the detrimental effect of plastic deformation on passivity then corrosion resistance as it was shown in previous reports[27–30].

One-time constant is shown in Bode plots, and the plateaus in the high-frequency range represent electrolyte resistance R_S[26]. As the frequency decreases, the impedances increase, and negative phase angles are detected, suggesting that capacitance dominates. The phase angles increase to remain maxima in a relatively wide range of frequencies and then decrease (Fig. 1c). However, this maxima value is still smaller than 90° in these three cases, which indicates a non-ideal capacitance behavior due to the capacitance dispersion. A constant phase element (CPE), Q_{CPE}, is therefore employed to present the distribution of interfacial capacitance originating from surface roughness or heterogeneities, especially on the atomic scale, fractal geometry, electrode porosity, non-uniform potential, and current distribution associated with the geometry of electrode[31,32]. The impedance of CPE is:

$$Z_{CPE} = \frac{1}{Q_{CPE}(j\omega)^n} \tag{1}$$

where j is the imaginary number, and ω is the angular frequency. Q_{CPE} is a constant independent of frequency and proportional to the active exposed area to the electrolyte. n is a dimensionless power number describing the deviation from the ideal capacitive behavior of capacitors, i.e., the closer the n to 1, the closer the CPE to pure capacitance while it presents resistor if n is close to zero. A slight deviation of n close to 1 means a non-ideal capacitance behavior of the surface after the polarization test. Q_{CPE} of the cold-rolled SDSS is seen to be much higher than that of its counterparts, implying a less homogeneous surface quality.

In line with most anti-corrosive features of the stainless steel, the relatively high Cr content in SDSS generally leads to the superior corrosion resistance of SDSS, which results from the presence of a passive thus protective oxide film on the surface[17]. Such a passive film generally has rich Cr^{3+} oxide and/or hydroxide with the integration of mainly Fe^{2+}, Fe^{3+} oxides, and/or (oxy) hydroxides[33]. Despite similar surface uniformity, passive oxide layers, and no observable breakdowns on the surfaces according to micrographic determinations[6,7], the corrosion behaviors differ in hot-deformed and cold-rolled SDSS, thus, requiring in-depth studies of microstructural features of the deformed steels.

Microstructural features

Microstructures of the deformed stainless steels were quantitatively studied via in-house and synchrotron high-energy X-ray radiation (Supplementary Figs. 1, 2). The detailed analysis is given in the Supplementary Information. Despite general agreements with the type of principal phases, differences in volume phase fraction are found and tabulated in Supplementary Table 1. The differences can be attributed to uneven phase fractions on the surface and in bulk subjected to different detection depths of the X-ray diffraction (XRD) with different sources of incident photon energies[34]. The relatively high austenite fraction in the cold-rolled sample quantified by lab-source XRD suggests better passivity then better corrosion resistance[35], while more accurate and statistical results from high-energy synchrotron XRD (HE-SXRD) imply an opposite trend regarding phase fractions. Besides this, the corrosion resistance of steels also depends on the extent of grain refinement, decrease in grain size, increase in microstrain, and dislocation density induced during thermomechanical processing[36–38]. The hot-deformed sample shows a more grainy nature indicating the micron-sized grains, whereas observed smooth rings in the cold-rolled sample (Supplementary Fig. 3) infer a significant grain refinement into nanometer scale in the previous work[6] which should promote passive film formation and improve corrosion resistance. The larger dislocation density usually correlates with worse pitting corrosion resistance, which matches well with the electrochemical measurement results.

Spectro-microscopic chemical inhomogeneities

Variations of microregional chemical states of essential elements were systematically examined via X-PEEM. Despite a large number of alloying elements, Cr, Fe, Ni, and Ce[39] were chosen here because Cr is the key element for passive film formation, Fe is the main element of steel, Ni enhances the passivity and balances the ferrite-austenite phase structure and Ce by its modification purpose. By tuning the synchrotron beam energy, the XAS covered the main features of Cr ($L_{2,3}$ edge), Fe ($L_{2,3}$ edge), Ni ($L_{2,3}$ edge), and Ce ($M_{4,5}$ edge) from the surface for both the hot-deformed and cold-rolled Ce-2507 SDSS. The respective data analysis was carried out by including the energy calibration with the published data, for example, XAS at the Fe $L_{2,3}$ edges[40,41].

Figure 2 shows the X-PEEM images of the hot-deformed (Fig. 2a) and cold-rolled (Fig. 2d) Ce-2507 SDSS along with corresponding Cr and Fe $L_{2,3}$ edge XAS at individually marked positions. $L_{2,3}$ edge XAS probes the unoccupied 3d states after photoexcitations of electrons at the spin-orbit split levels $2p_{3/2}$ (L_3 edge) and $2p_{1/2}$ (L_2 edge). The information about the Cr valence states is obtained from XAS at the $L_{2,3}$ edge in Fig. 2b, e. A comparison with the refs. [42,43] suggests the observation of four peaks referred to A (578.3 eV), B (579.5 eV), C (580.4 eV), and D (582.2 eV) next to the L_3 edge reflecting the octahedral Cr^{3+} ion corresponding to Cr_2O_3. The experimental spectra agree with theoretical simulations as shown in panels b and e given by a crystal field multiplet calculation of the Cr $L_{2,3}$ edge, using a crystal field of 2.0 eV[44]. Both surfaces of hot-deformed and cold-rolled SDSS are covered with relatively uniform Cr_2O_3 layers.

Chemical states of the alloying element Ni and the Ce additive are kept the same for both samples, regardless of the chemical environment of these metal elements. Supplementary Figs. 5–9 show the X-PEEM image and corresponding XAS spectra at various locations for Ni and Ce on surfaces of hot-deformed and cold-rolled samples. Ni XAS shows Ni^{2+} oxidation state throughout the measured surface in both hot-deformed and cold-rolled samples (Supplementary Discussion). It is noted that no XAS signal could be observed for Ce in the case of the hot-deformed sample, whereas Ce^{3+} spectrum is observed for the cold-rolled specimen at a spot. The observation of Ce spot in cold-rolled samples suggests that Ce mainly occurs as precipitates.

No local structural changes in the XAS at the Fe $L_{2,3}$ edges are observed in hot-deformed SDSS (Fig. 2c). However, the Fe matrix varies its chemical states micro-regionally in the seven randomly selected spots for cold-rolled SDSS, as revealed in Fig. 2f. Furthermore, to have an exact picture of Fe state variation in the chosen sites in Fig. 2f, local surface investigations have been implemented (Fig. 3 and Supplementary Fig. 10), wherein smaller circular regions were chosen. The Fe $L_{2,3}$ edge XAS spectra of α-Fe_2O_3 and an octahedral Fe^{2+} oxide system have been simulated with crystal field multiplet calculations, using crystal fields of 1.0 (Fe^{2+}) and 1.0 (Fe^{3+})[44]. We note that α-Fe_2O_3 and γ-Fe_2O_3 have different local symmetries[45,46], Fe_3O_4 has combination of both Fe^{2+} & Fe^{3+}[47], and FeO[45] as a formally divalent Fe^{2+} oxide ($3d^6$). All Fe^{3+} ions in α-Fe_2O_3 have the O_h sites only, while γ-Fe_2O_3 is often represented by Fe^{3+} t_{2g} [Fe^{3+} $_{5/3}V_{1/3}$]e_g O_4 spinel with vacancies at e_g sites. Hence Fe^{3+} ions in γ-Fe_2O_3 have both the T_d and O_h sites. As mentioned in the previous work[45], although the intensity ratio for both these is different, their intensity ratio of e_g/t_{2g} is »1, whereas, in the present case, the observed intensity ratio of e_g/t_{2g} is ~1. This excludes the possibility of only Fe^{3+} in the present case. Considering the case of Fe_3O_4 which has a combination of both Fe^{2+} and Fe^{3+}, it is known that weaker (stronger) first feature in L_3 edge of Fe is indicative of less (more) un-occupancy in t_{2g} state. This is the case for Fe^{2+} (Fe^{3+}), suggesting that an increased first feature is indicative of increased Fe^{2+} content[47]. These results indicate the coexistence of Fe^{2+} and
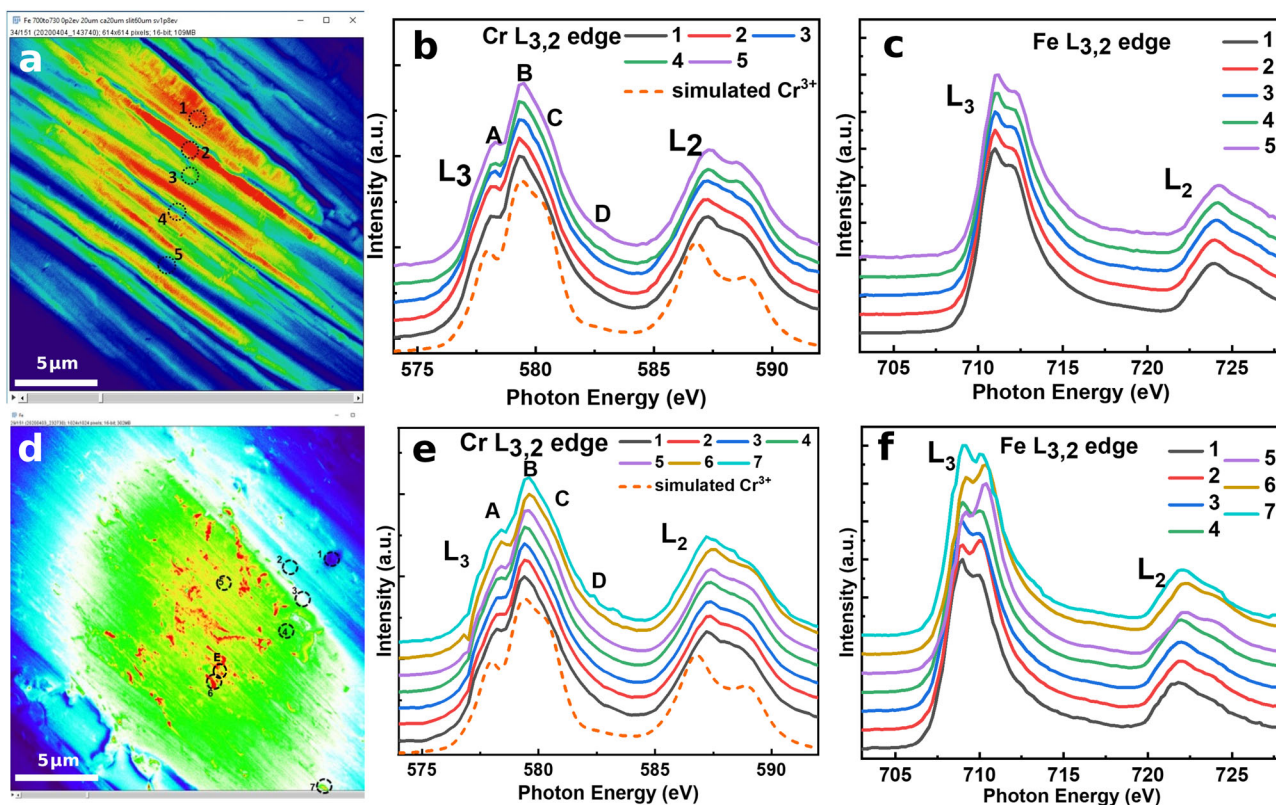
Fig. 2 X-PEEM of SDSS. a X-PEEM thermal image of hot-deformed SDSS, corresponding **b** Cr $L_{2,3}$ edge and **c** Fe $L_{2,3}$ edge, **d** X-PEEM thermal image of cold-rolled SDSS, corresponding **e** Cr $L_{2,3}$ edge and **f** Fe $L_{2,3}$ edge (**f**). XAS spectra are plotted at various spatial positions as marked in the thermal image (**a**, **d**), and the orange dashed line in (**b**) and (**e**) represents the simulated Cr^{3+} XAS spectrum with a crystal field value of 2.0 eV. For X-PEEM images, a thermal color palette is used to improve the image readability in which the colors, from blue to red, is proportional to the X-ray absorption intensity (low to high).

γ-Fe_2O_3, α-Fe_2O_3, and or Fe_3O_4 dominates composites on the cold-rolled surface.

The obtained experimental data were plotted (Fig. 4a and Supplementary Fig. 11) and compared with those of pure compounds[40,41,48]. Mainly three distinct types of experimentally observed Fe L-edge XAS spectra (XAS-1, XAS-2, and XAS-3: Fig. 4a) have been noted at spatially different locations. In particular, spectrum like 2-a in Fig. 3b (referred to as XAS-1) has been observed throughout the probed area followed by the spectrum 2-b (referred to as XAS-2), whereas spectrum like E-3 in Fig. 3d (referred to as XAS-3) is observed at certain local positions. Typically, four parameters have been used to identify the existing valence states in the probed sample: (1) spectral features of L_3 and L_2, (2) energy positions of L_3 and L_2 features, (3) the energy difference of L_3-L_2, and (4) the intensity ratio of L_2/L_3. As per the visual observation (Fig. 4a), all three components of Fe, that is, Fe^0, Fe^{2+}, and Fe^{3+} are present on the surface of probed SDSS. The calculated intensity ratio of L_2/L_3 also suggests the presence of all three components.

Linear combination fitting (LCF) of the three standards[40,41,48] are employed to have a quantitative picture of iron oxide compositions. LCF has been implemented for the three chosen Fe L-edge XAS spectra showing the highest contrast, that is, XAS-1, XAS-2, and XAS-3, as shown in Fig. 4b–d. For the LCF fitting, 10% Fe^0 is considered for all the cases as we have observed a small shoulder in all the data along with the fact that Fe metal is the main component of steel. Indeed, the probation depth of X-PEEM for Fe (~6 nm)[49] is bigger than the estimated oxidation layer thickness (slightly > 4 nm), allowing detection of signal from the iron matrix (Fe^0) beneath the passivation layer. Different combinations of Fe^{2+} and Fe^{3+} were carried out to find the best

possible solution for the observed experimental data. Figure 4b shows the combination of Fe^{2+} and Fe^{3+} for the XAS-1 spectrum, wherein the fractions of Fe^{2+} and Fe^{3+} are found similar ~45%, suggesting a mixed oxidation state of Fe. Whereas, for the XAS-2 spectrum, the percentage of Fe^{2+} and Fe^{3+} respectively changes to ~30 and 60%. The Fe^{2+} is less abundant than the Fe^{3+}. The ratio of 1:2 for Fe^{2+} to Fe^3 refers to the possible formation of Fe_3O_4 which has the same ratio between the Fe ions. Furthermore, for the spectrum the XAS-3, the percentages of Fe^{2+} and Fe^{3+} change to ~10 and 80%, suggesting higher conversion of Fe^{2+} to Fe^{3+}. As noticed above, the Fe^{3+} may originate from α-Fe_2O_3, γ-Fe_2O_3, or Fe_3O_4. To understand the most probable origin of Fe^{3+}, the XAS-3 spectrum is plotted along with different Fe^{3+} standards in Fig. 4e showing similarity with all the two standards when considering peak B. However, the intensity of shoulder peak (A: arise from Fe^{2+}) and intensity ratio of B/A suggest that XAS-3 spectrum is close to but not well matched with that of γ-Fe_2O_3. Compared to bulk γ-Fe_2O_3, the Fe 2p XAS for SDSS exhibits a slightly higher intensity for peak A (Fig. 4e), suggesting higher intensity of Fe^{2+}. Despite the similarity of XAS-3 spectrum with γ-Fe_2O_3, wherein Fe^{3+} exist both at O_h and T_d site, such identifications of different valence state and coordination solely from $L_{2,3}$ edge or L_2/L_3 intensity ratio are still a subject of ongoing discussion due to the complexity of various factors affecting the final spectrum[41].

Global chemical inhomogeneities

In addition to the above spectroscopic distinctions of chemical states at selected regions of interest, global chemical heterogeneities of key elements, Cr and Fe, have been assessed by using a K-means clustering method to classify all XAS spectra obtained on the sample surfaces. Profiles of Cr L edge are set to form two
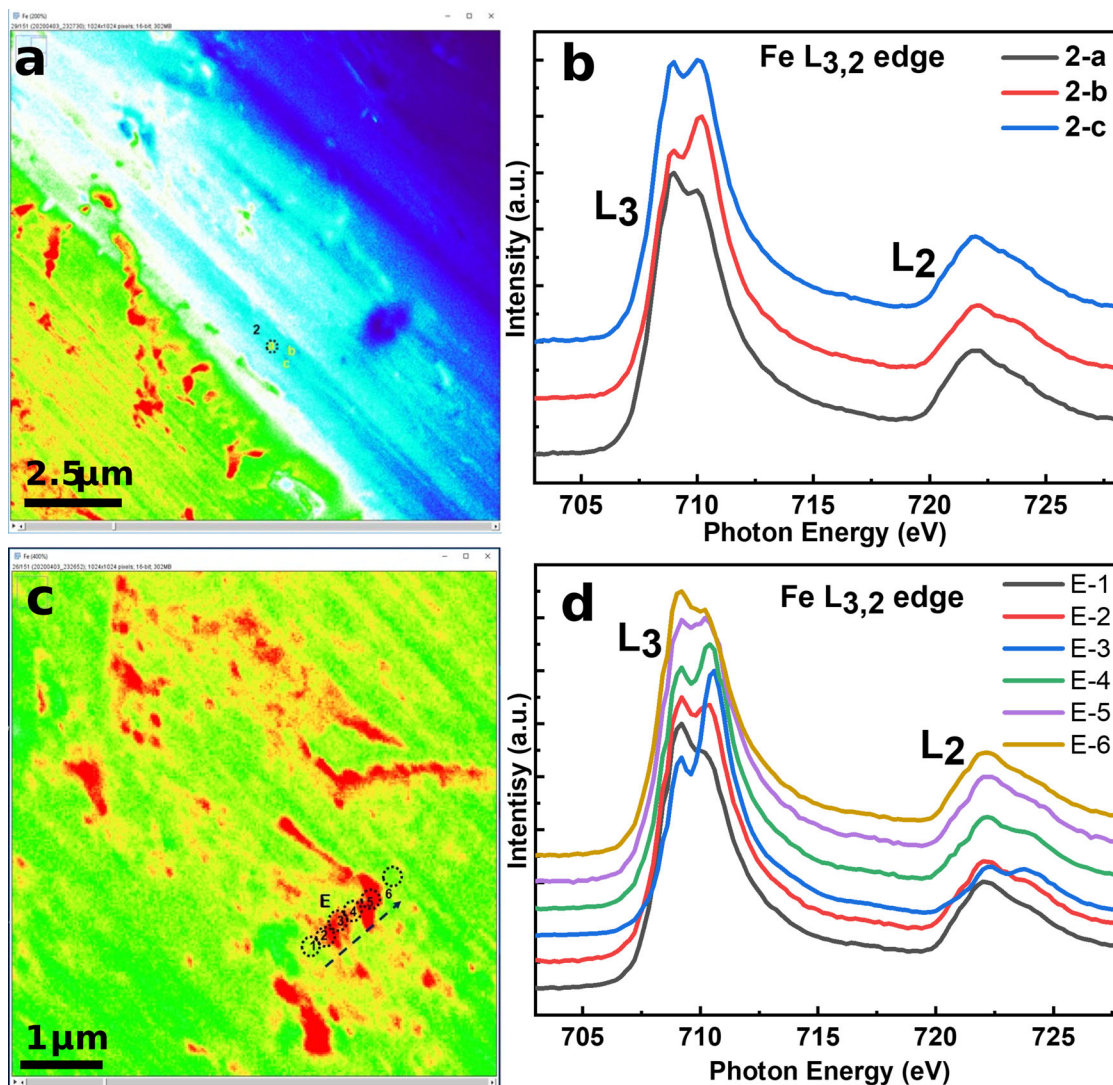
Fig. 3 Enlarged X-PEEM of SDSS. The enlarged photoemission electron thermal image (**a**, **c**) and (**b**, **d**) XAS spectra crossing Fe $L_{2,3}$ edge at various spatial positions within the chosen region 2 and E of Fig. 2d.

optimal clusters spatially distributed in both hot-deformed and cold-rolled samples shown in Fig. 5. It is evident that no local structural changes are perceived since the two centroids of Cr XAS spectra are rather similar. The shapes of these spectra for two clusters are nearly identical to those corresponding to Cr_2O_3[42], meaning the Cr_2O_3 layers are relatively evenly placed on the SDSS.

For the illustration of a more complex Fe L edge map, four and five optimized clusters along with their related centroids (spectral profiles) are used for hot-deformed and cold-rolled samples, respectively. Accordingly, the percentage (%) of Fe^{2+} and Fe^{3+} can be obtained by the LCF fitting shown in Fig. 4. A pseudo electrode potential E_{pseudo} vs. Fe^0 is applied to elucidate the microscopical chemical inhomogeneity of the surface oxide film. The E_{pseudo} is roughly estimated by the rule of mixtures,

$$E_{pseudo} = E_{Fe/Fe^{2+}} \times \%_{Fe^{2+}} + E_{Fe/Fe^{3+}} \times \%_{Fe^{3+}} \qquad (2)$$

wherein, $E_{Fe/Fe^{2+(3+)}}$ is the standard electrode potential for $Fe + 2e^- \rightarrow Fe^{2+(3+)}$, 0.440 and 0.036 V, respectively. The region with a lower potential has a higher content of Fe^{3+} compounds. The potential profile in the hot-deformed sample shows a lamellar-like distribution with a maximal variation of about 0.119 V (Fig. 6a, b). This potential distribution is closely related to the surface topography (Fig. 6a). No other position-related change inside the potential lamellar is observed (Fig. 6b). In contrast, the non-uniform character of the pseudopotential can be observed in the cold-rolled SDSS (Fig. 6c, d) for connections of dissimilar oxide with different Fe^{2+} and Fe^{3+} contents. Fe^{3+} oxide and/or (oxy)hydroxide are the main constituents of rust in steels and are permeable to oxygen and water[50]. Fe^{3+} rich islands are seen to be distributed locally in this case and can be considered as already-corroding areas. Meanwhile, the gradients in the potential field not the absolute values of potentials can be considered as an indicator to locate actively corroding areas[51]. This uneven distributions of Fe^{2+} and Fe^{3+} on the surface of cold-rolled SDSS could modify the local chemistry and provide more actual active surface areas in the breakdown of oxide films and corrosion reaction to allow continuous corrosion of metallic matrix beneath, leading to intrinsic heterogeneity and reducing the protective performance of the passive layer.

Corrosion due to chemical inhomogeneity of Fe

The relatively uniform Cr but varied Fe chemical states place a different origin of oxide film breakdown and corrosion scheme in the hot-deformed and cold-rolled Ce-2507. A detailed insight has been drawn to understand this property of cold-rolled Ce-2507.
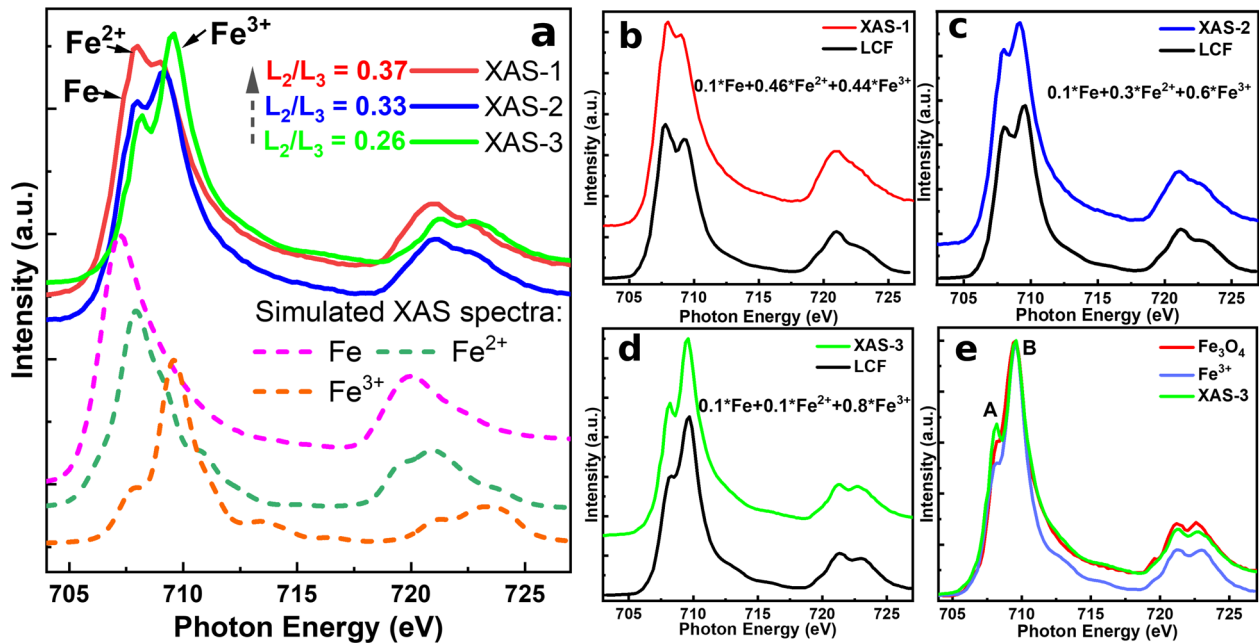
Fig. 4 Analysis of XAS spectra. a Comparison of observed distinct three experimental data (solid lines XAS-1, XAS-2, and XAS-3 correspond to 2-a, 2-b and E-3 in Figs. 2 and 3) with the simulated XAS spectra for Fe, Fe^{2+}, Fe^{3+} octahedral with a crystal field value of 1.0 eV and 1.5 eV, respectively; **b–d** Measured experimental data (XAS-1, XAS-2, XAS-3) and the corresponding optimized LCF data (black solid line), and **e** comparison of XAS-3 spectrum with Fe_3O_4 (mixed Fe states) and Fe_2O_3 (pure Fe^{3+}) standards.

Regarding the formation of Fe oxides and hydroxides in ambient air in this work that is closed to be neutral, the reaction is:
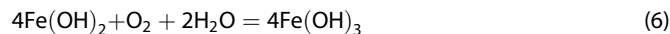
Anodic:

$$Fe = Fe^{2+} + 2e^- \tag{3}$$

Cathodic reaction due to the absorption layer of water with dissolved O_2[52]:

$$O_2 + 2H_2O + 4e^- = 4OH^- \tag{4}$$

and at sites forming Fe hydroxides,

$$Fe^{2+} + 2OH^- = Fe(OH)_2 \tag{5}$$

With more dissolved oxygen, oxidation from Fe^{2+} to Fe^{3+} happens via

$$4Fe(OH)_2 + O_2 + 2H_2O = 4Fe(OH)_3 \tag{6}$$

wherein, $Fe(OH)_2$ and $Fe(OH)_3$ can dehydrate to generate FeO, Fe_2O_3, and Fe_3O_4.

The above reactions happened in the following scenario based on X-PEEM determinations. The small shoulder corresponding to Fe^0 is due to metallic iron beneath. The reaction of Fe metal with the environment gives rise to a layer of $Fe(OH)_2$ (Eq. (5)), raising the Fe^{2+} signal in Fe L-edge XAS. Continuous exposure to the air leads to the formation of Fe_3O_4 and or Fe_2O_3 oxides following $Fe(OH)_2$[52,53]. The two stable species of Fe, i.e., Fe_3O_4 and Fe_2O_3 could also be formed in the Cr^{3+} rich protective layer, of which Fe_3O_4 prefers a homogeneous and adherent structure. The presence of both can give rise to mixed oxidation states (XAS-1 spectrum). The XAS-2 spectrum corresponds to mainly Fe_3O_4. Whereas observation of the XAS-3 spectrum at a few locations suggests the complete conversion to γ-Fe_2O_3. A higher intensity of peak A is resulted from signals from a beneath layer as the deployed X-ray has a penetration depth of ~50 nm.

XAS spectra suggest Fe components in the oxide films having a layered structure, integrating with the Cr oxide layer. In contrast to passivation features due to the local inhomogeneity of Cr_2O_3 for corrosion[17], low corrosion resistance, especially for the cold-rolled

sample is observed in the present case despite the homogenous Cr_2O_3 layer in this work. The observed behavior can be understood as the non-uniformity in the chemical oxidation state in the top layer (Fe) affecting the corrosion properties. Since homogenous stoichiometry of the top layer (Fe oxide) and the beneath layer (Cr oxide)[52,53] give rise to better interaction (adhesion) between the two, leading to slow transport of metal or oxygen ions in the lattice, which in turn will increase the corrosion resistance. Thus, a continuous stoichiometry, that is, a single oxidation state of Fe is preferred over an abrupt stoichiometry change. For the hot-deformed SDSS, the surface is more uniform with a denser protective layer leading to better corrosion resistance. Whereas, for the cold-rolled SDSS, the existence of Fe^{3+} rich islands beneath the protective layer destroy the integrity of the surface and produce a galvanic corrosion with the nearby matrix, which leads to the drastic decrease of the R_p (Table 1) in the EIS spectrum and reduction of its corrosion resistance. Thus, Fe^{3+} rich islands distributed locally due to plastic deformation, primarily affect the corrosion resistance performance, a breakthrough of this work. This study thus provides a spectro-microscopic picture of corrosion resistance reduction in the studied SDSS samples by plastic deformation.

Moreover, even though rare earth alloying in duplex steel shows the betterment in their performances, the interaction of this additive element with the steel matrix individuals in regard to corrosion behavior remains elusive according to the spectro-microscopic observations. Appearances of the Ce signal (via M edge XAS) only at a few locations in the cold-rolled but vanishing in the hot-deformed SDSS suggest the local precipitation of Ce in the steel matrix rather than the homogenous alloying. Though not bringing substantial enhancements to mechanical properties of SDSS[6,7], the presence of the rare-earth element reduces sizes of inclusion and is believed to suppress pitting corrosion at the initial sites[54].

To summarize, this work unveils the impacts of surface inhomogeneity on corrosion of the Ce-modified 2507 SDSS by quantifying the chemical abundances of the compositions at the nanoscale. We answered a question that why stainless steels
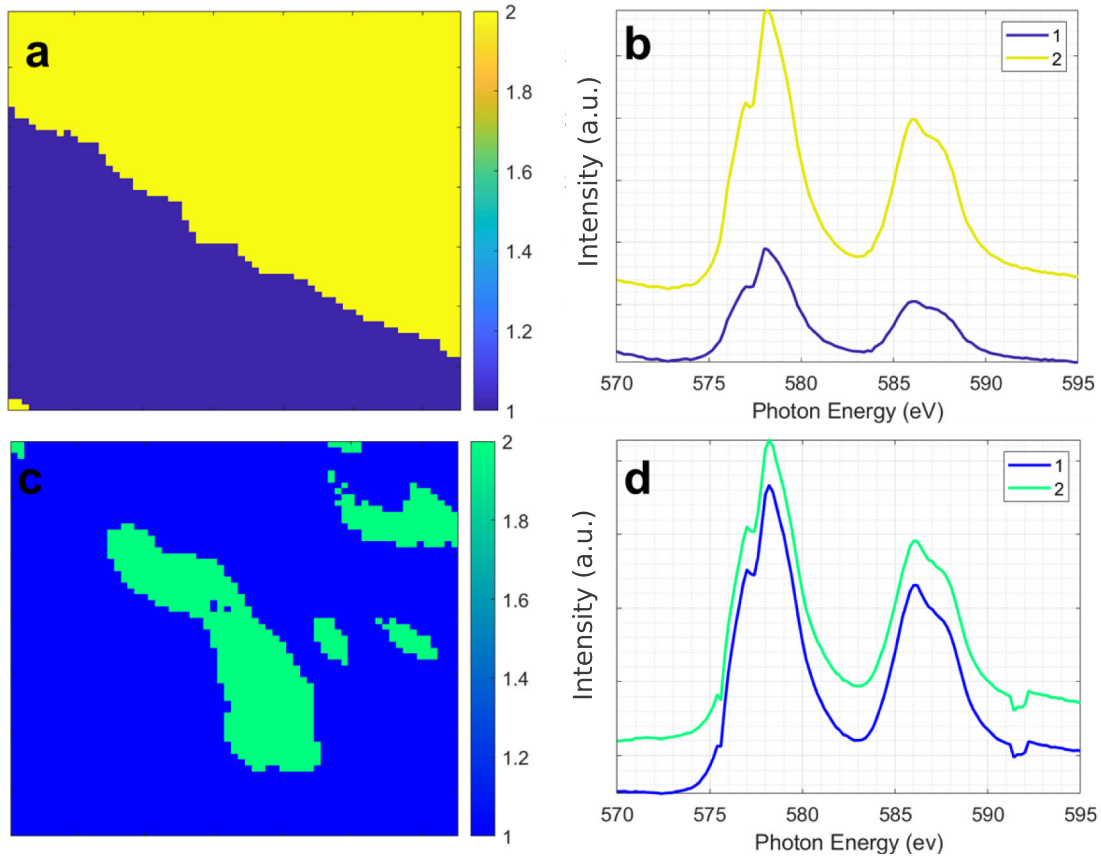
Fig. 5 Cr mapping of hot-deformed and cold-rolled SDSS. a K-means cluster of the Cr L-edge region, and **b** corresponding XAS centroids. K-means mapping results of X-PEEM for cold-rolled SDSS: **c** K-means cluster of the Cr $L_{2,3}$-edge region, and **d** corresponding XAS centroids.
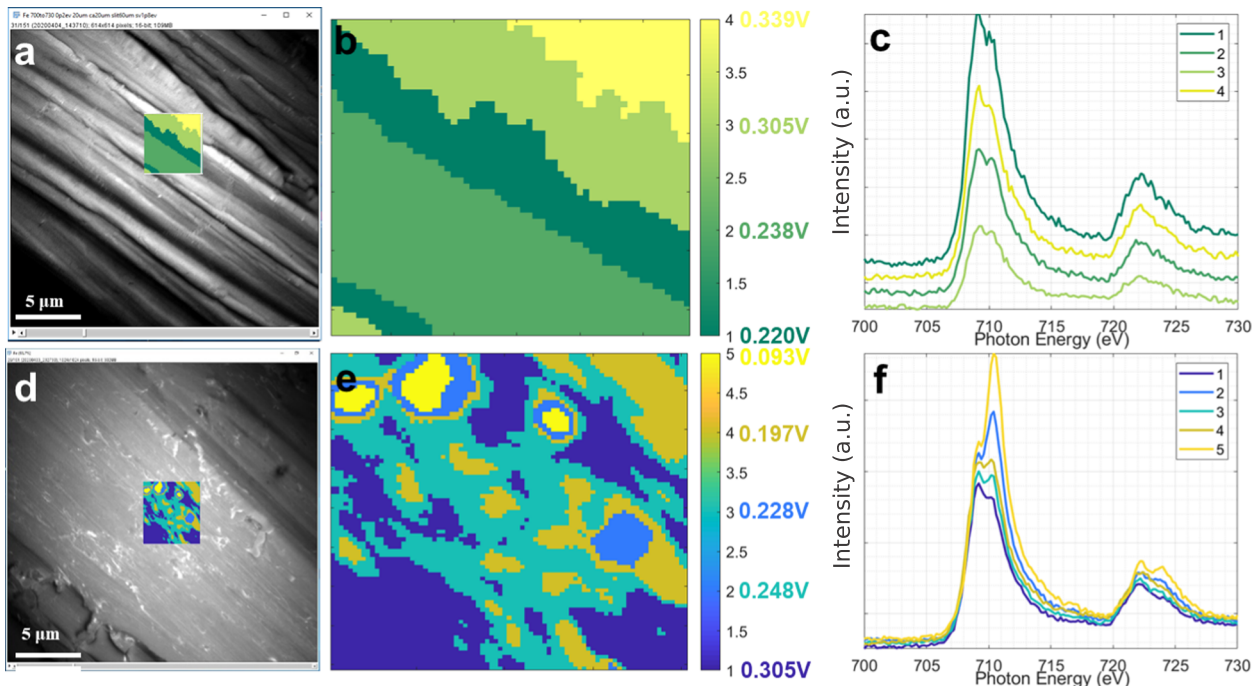

Fig. 6 Fe mapping of hot-deformed and cold-rolled SDSS. K-means cluster of the Fe $L_{2,3}$-edge region and corresponding XAS centroids for **a–c** hot-deformed and **d–f** cold-rolled SDSS of X-PEEM. **a, d** The K-means cluster map superimposed on X-PEEM image. Calculated pseudo electrode potential (E_{pseudo}) is mentioned along with K-means cluster map. Brightness, like the colors in Fig. 2, in the X-PEEM image is proportional to the X-ray absorption intensity.

corrode even when they are covered with protective oxide layers via quantitively investigating their microstructures, element chemical states on surfaces, and using the signal processing method of K-means clustering. It is found that the Fe^{3+} rich islands, including its octahedral and tetrahedral coordination over the throughout features of mixed Fe^{2+}/Fe^{3+}, serve as the breakdown source of oxide film then the source of corrosion in cold-rolled SDSS. The Fe^{3+} dominated nano-islands lead to a poor corrosion resistance even in the presence of adequate stoichiometric Cr_2O_3 passive layers. Besides methodological progress in identifying the impact of nano-scaled chemical inhomogeneity on corrosion, the present work is hoped to inspire engineering processes to enhance the corrosion resistance of stainless steels during steelmaking.

METHODS

Materials

To prepare Ce-2507 SDSS ingot for this study, mixed ingredients including Fe-Ce master alloy sealed by pure iron pipe were melted in a 150 kg intermediate frequency induction furnace to obtain molten steel and poured into a cast mould. The measured chemical composition (wt.%) is listed in Supplementary Table 2. The cast ingots were hot forged into blocks first. Subsequently, the steel in a solid solution state was obtained by annealing at 1050 °C for 60 min, and then was water quenched to room temperature. The studied samples have been investigated in detail using TEM and EBSD to study the phases, grain sizes, and morphology. More details about the sample and the production process can be found elsewhere[6,7].

Deformation at different temperatures

Cylindrical specimens (ϕ10 mm × 15 mm) for hot-compression were machined with the axes of the cylinder being parallel to the deformation direction of the block. High-temperature compression was carried out using Gleeble-3800 thermo-simulation machine at various temperatures such as 1000–1150 °C under constant strain rates in the range of $0.01–10 \, s^{-1}$. Before deformation, specimens were heated at chosen temperatures at the rate of $10 \, °C \, s^{-1}$ and held for 2 min to eliminate any thermal gradients. After attaining temperature uniformities, the specimens were deformed to a true strain value of 0.7. After deformations, the specimens were immediately quenched by water to retain the deformed structure. The quenched specimens were then cut parallel to the compression direction. For this particular study, we have chosen specimens with hot deformation conditions as 1050 °C, $10 \, s^{-1}$ because of the observed higher microhardness than other samples[7].

A three-phase asynchronous two-high deformation mill LG-300 was used to conduct room temperature cold rolling up to a deformation level of 90% (engineering strain) for the solid-solution Ce-2507 block-shaped ($80 \times 10 \times 17 \, mm^3$) specimen, which gives the best mechanical performances among all other levels of deformation[6]. The deformation speed and the thickness reduction per single path were used as $0.2 \, m \, s^{-1}$ and 5%, respectively.

Electrochemical measurements

The Autolab PGSTAT128N electrochemical workstation was employed to perform electrochemical measurements of the SDSS after cold rolling to a 90% thickness reduction (equivalent true stain is 1.0) and after hot compression to a true strain value of 0.7 at 1050 °C, 10 s^{-1}. The workstation has a three-electrode cell with a saturated calomel electrode as the reference electrode, a graphite counter electrode, and the SDSS specimens as the working electrode. Samples were cut into ϕ11.3 mm cylinders with a Cu wire soldered to the lateral side. Then the samples were mounted into epoxy resin, leaving a working exposure area of $1 \, cm^2$ as the working electrode (bottom surface of the cylindrical samples). To avoid producing crevices, care was taken during the curing of epoxy resin and following grinding and polishing procedures. The working surfaces were ground and polished using 1 μm diamond polishing suspension, cleaned with distilled water and ethanol, and dried in cool air. Prior to the electrochemical measurements, the as-polished samples were allowed to stand in ambient air for days for a naturally formed oxide film. Hydrous $FeCl_3$ (6.0 wt%) solution stabilized by HCl to a $pH = 1.0 \pm 0.01$ was used to promote

corrosion of stainless steels[55] due to its aggressive environment in the presence of chloride ions with the strong oxidizing ability and low pH, as suggested by ASTM G48 and A923 standards. The specimens were immersed in the test solution for 1 h before any measurement to achieve near-steady state. The impedance measurements ranged from the frequencies of $1 \times 10^5 \sim 0.1$ Hz with an amplitude of 5 mV at open circuit potential (OCP) of 0.39, 0.33, and 0.25 V_{SCE} for solid solution, hot-deformed, and cold-rolled sample, respectively. Each electrochemical test for any specimen had been repeated at least three times under identical conditions to ensure data reproducibility.

HE-SXRD and X-PEEM

To carry out HE-SXRD measurements, rectangular blocks of dimension $1 \times 1 \times 1.5 \, mm^3$ duplex steels were measured to quantify the phase constituents at the Brockhouse High Energy Wiggler Beamline, CLS, Canada[56]. The data collection was performed in Debye-Scherrer or transmission geometry at room temperature. The X-ray wavelength calibrated from a LaB_6 calibrant was 0.212561 Å corresponding to 58 keV much higher than the one of Cu Kα (8 keV) conventionally used as the incident source of lab XRD. The sample was placed at a distance of 740 mm from the detector. The probed volume of each specimen was $0.2 \times 0.3 \times 1.5 \, mm^3$, determined by the beam size and thickness of the specimen. An exposure time of 0.3 s was used along with 120 frames for each of these data collection using a Perkin Elmer area detector, a flat panel x-ray detector, 200 μm pixel, $40 \times 40 \, cm^2$.

The X-PEEM measurement on these two selected model systems was carried out at the PEEM endstation of Beamline MAXPEEM at MAX IV laboratory (Lund, Sweden). Samples were prepared in the same way as that for electrochemical measurements. Before being exposed to synchrotron photons, the as-prepared samples had been aged in ambient air for days and degassed in an ultrahigh vacuum chamber. The energy resolution of the beamline was obtained by measuring the ion yield spectrum at the N 1s to $1\pi_g^*$ excitation region around $h\nu = 401$ eV in N_2 with photon energy dependence of $E^{3/2}$[57]. The fit of the spectrum gave a ΔE (spectrum linewidth) of ~0.3 eV at the measured energy range. Therefore, the beamline energy resolution was estimated to be $E/\Delta E = 700$ eV/ 0.3 eV > 2000 and flux $\approx 10^{12}$ ph/s by utilizing a modified SX-700 monochromator with a Si 1200-line mm^{-1} grating for the Fe 2p $L_{2,3}$ edge, Cr 2p $L_{2,3}$ edge, Ni 2p $L_{2,3}$ edge, and Ce $M_{4,5}$ edge. The photon energy was scanned with a 0.2 eV step. At each energy, a PEEM image was recorded with a TVIPS F-216 optical fiber-coupled CMOS detector with 2 by 2 binning, which provides 1024×1024 pixels in the field of view of 20 μm. The exposure time of images was 0.2 s with an average number of 16 frames. The imaging energy of photoelectrons was chosen to provide the highest secondary electron signal. All measurements were performed at perpendicular incidence angles with linearly polarized photon beams. More details of the measurements can be found in the previous study[58]. Probation depths of the present method are estimated to ~ 4–5 nm for Cr signal and ~ 6 nm for Fe following studies of the total electron yield (TEY) detection mode[59] and its application in the X-PEEM[49]. The depth for Cr is very close to oxidation film thickness (~4 nm)[60,61] and the one for Fe is more than the thickness. The XAS collected next to the Fe L-edges is a mixture of XAS of the iron oxides and Fe^0 from the matrix. In the former case, intensities of emitted electrons arise from all possible types of electrons which contribute to the TEY. As for the signal of the pure iron, however, electrons require higher kinetic energies to pass through oxide layer, reach the surface and then are collected by the analyzer. In this case, the Fe^0 signal is mainly due to LVV Auger electrons, and the secondary electrons ejected by them[49]. Moreover, TEY intensities contributed by these electrons are attenuated during the electron escaping paths[49], further lowering the Fe^0 spectral signatures in the iron XAS plots.

K-means clustering for statistical map of XAS spectra

The integration of data mining in the data cube (X-PEEM data) is a crucial step to extract the relevant information (chemical or physical properties) in a multivariate approach. The K-means clustering has widely been applied in several fields, including machine vision, image processing, unsupervised pattern recognition, artificial intelligence, and classification analysis[24]. For instance, the K-means clustering was well-established in hyperspectral image data clustering[62]. In principle, for data with several objects, the K-means algorithm could easily cluster them based on their attribute's information (photon energy characteristic). The K-means clustering is an iterative algorithm for portioning the data into K disjoint groups (clusters),

where each pixel belongs to a specific cluster depending on the spatial distribution of the chemical heterogenty in the steel microstructure composition. K-means algorithm involves two phases: in the first phase, the K centroid is calculated, while in the second phase, each point is assigned to the cluster which has an adjacent centroid. The cluster centroid is defined as an arithmetic mean of the data points (XAS spectra) of that cluster. Different distances exist to define the adjacent centroid as the Euclidean distance. For an input image $p_{x,y}$ (with x and y are pixels resolution), and the C_K is cluster centroids; then this image can be segmented (clustered) into K clusters by K-means[63]. The summarized steps of the algorithm for K-means clustering are:

Step 1. Define the data partition by selecting the K cluster centroids.

Step 2. Calculate the memberships of all pixels based on the current centroids. For example, it is calculated by Euclidean distance, d, between the center and each pixel:

$$d = \left\| p_{x,y} - C_K \right\| \tag{7}$$

Step 3. Assign each pixel to the closest centroid. Then recalculate the positions of the K centroids as follows:

$$C_k = \frac{1}{k} \sum_{y \in C_k} \sum_{x \in C_k} p_{x,y} \tag{8}$$

Step 4. Repeat the process (Eqs. (7) and (8)) until the convergence of centroids. The final clustering quality results are highly related to the optimum selection of the initial centroid[63]. For the structure of steel image PEEM data, in general, X ($x \times y \times \lambda$) is a 3-D array data cube, while x and y axes represent spatial information (pixels resolution) and the λ axis corresponds to the photon energy spectral pattern. The K-means algorithm is used to investigate the region of interest in X-PEEM data by employing the partitioning of pixels (cluster or sub-pieces) according to their spectral signature and extract the best centroid (XAS spectral profiles) for each analyte (cluster). It is applied to study the spatial distribution, local spectroscopic variation, oxidation behavior, and chemical state. The K-means cluster algorithm is, for instance, used for Fe L-edge and Cr L-edge regions in the hot-deformed and cold-rolled X-PEEM. Different number of K clusters (microstructural regions) were tested to find the optimum clusters and centroids. Displaying the figures, the pixels were reassigned to the proper cluster centroids. Each color distribution corresponded to one cluster center exhibiting the spatial arrangement of chemical or physical entities. The extracted centroids are linear combinations of the pure spectra.

DATA AVAILABILITY

The data that support the findings of this study are available from the corresponding author, W.C., upon reasonable request.

REFERENCES

1. Sieurin, H. & Sandström, R. Fracture toughness of a welded duplex stainless steel. *Eng. Fract. Mech.* **73**, 377–390 (2006).
2. Adams, F. V., Olubambi, P. A., Potgieter, J. H. & Van Der Merwe, J. Corrosion resistance of duplex stainless steels in selected organic acids and organic acid/chloride environments. *Anti-Corros. Methods Mater* **57**, 107–117 (2010).
3. Barella, S. et al. Corrosion and oxidation behavior of a Fe-Al-Mn-C duplex alloy. *Materials* **12**, 2572 (2019).
4. Levkov, L., Shurygin, D., Dub, V., Kosyrev, K. & Balikoev, A. New generation of super duplex steels for equipment gas and oil production. *E3S Web Conf.* **121**, 04007 (2019).
5. Kingklang, S. & Uthaisangsuk, V. Investigation of hot deformation behavior of duplex stainless steel grade 2507. *Metall. Mater. Trans. A* **48**, 95–108 (2017).
6. Zhou, T. et al. Controlled cold rolling effect on microstructure and mechanical properties of Ce-modified SAF 2507 super duplex stainless steel. *Mater. Sci. Eng. A* **766**, 138352 (2019).
7. Zhou, T. et al. Hot-deformation-induced structural and mechanical properties of Ce-modified SAF 2507 super duplex stainless steel. *J. Mater. Res. Technol.* **9**, 8379–8390 (2020).
8. Zheng, Z., Wang, S., Long, J., Wang, J. & Zheng, K. Effect of rare earth elements on high temperature oxidation behaviour of austenitic steel. *Corros. Sci.* **164**, 108359 (2020).
9. Li, Y., Yang, G., Jiang, Z., Chen, C. & Sun, S. Effects of Ce on the microstructure and properties of 27Cr-3.8Mo-2Ni super-ferritic stainless steels. *Ironmak. Steelmak* **47**, 67–76 (2020).
10. Li, M. et al. Study of biocompatibility of medical grade high nitrogen nickel-free austenitic stainless steel in vitro. *Mater. Sci. Eng. C* **43**, 641–648 (2014).
11. Vignal, V., Krawiec, H., Heintz, O. & Mainy, D. Passive properties of lean duplex stainless steels after long-term ageing in air studied using EBSD, AES, XPS and local electrochemical impedance spectroscopy. *Corros. Sci.* **67**, 109–117 (2013).
12. Wang, Y., Cheng, X. & Li, X. Electrochemical behavior and compositions of passive films formed on the constituent phases of duplex stainless steel without coupling. *Electrochem. Commun.* **57**, 56–60 (2015).
13. Gardin, E., Zanna, S., Seyeux, A., Allion-Maurer, A. & Marcus, P. Comparative study of the surface oxide films on lean duplex and corresponding single phase stainless steels by XPS and ToF-SIMS. *Corros. Sci.* **143**, 403–413 (2018).
14. Shi, X. et al. Quantitative assessment of structural and compositional colors induced by femtosecond laser: a case study on 301LN stainless steel surface. *Appl. Surf. Sci.* **484**, 655–662 (2019).
15. Lu, Y. et al. Nanosecond laser coloration on stainless steel surface. *Sci. Rep.* **7**, 7092 (2017).
16. Långberg, M. et al. Lateral variation of the native passive film on super duplex stainless steel resolved by synchrotron hard X-ray photoelectron emission microscopy. *Corros. Sci.* **174**, 108841 (2020).
17. Ma, L., Wiame, F., Maurice, V. & Marcus, P. Origin of nanoscale heterogeneity in the surface oxide film protecting stainless steel against corrosion. *npj Mater. Degrad.* **3**, 29 (2019).
18. Yamanaka, K. et al. Surface evolution and corrosion behaviour of Cu-doped carbide-reinforced martensitic steels in a sulfuric acid solution. *npj Mater. Degrad.* **5**, 43 (2021).
19. Pan, J. Studying the passivity and breakdown of duplex stainless steels at micrometer and nanometer scales – the influence of microstructure. *Front. Mater.* **7**, 133 (2020).
20. Långberg, M. et al. Redefining passivity breakdown of super duplex stainless steel by electrochemical operando synchrotron near surface X-ray analyses. *npj Mater. Degrad.* **3**, 22 (2019).
21. Maurice, V. & Marcus, P. Current developments of nanoscale insight into corrosion protection by passive oxide films. *Curr. Opin. Solid State Mater. Sci.* **22**, 156–167 (2018).
22. Singh, H. et al. Unveiling interactions of non-metallic inclusions within advanced ultra-high-strength steel: a spectro-microscopic determination and first-principles elucidation. *Scr. Mater.* **197**, 113791 (2021).
23. Shi, X. et al. Metallic contact between MoS₂ and Ni via Au nanoglue. *Small* **14**, 1704526 (2018).
24. Kodinariya, T. M. & Makwana, P. R. Review on determining of cluster in K-means clustering. *Int. J.* **1**, 90–95 (2016).
25. Jiang, P. et al. Microstructural influence on corrosion behavior of MgZnGe alloy in NaCl solution. *J. Alloys Compd.* **783**, 179–192 (2019).
26. Homayun, B. & Afshar, A. Microstructure, mechanical properties, corrosion behavior and cytotoxicity of Mg-Zn-Al-Ca alloys as biodegradable materials. *J. Alloys Compd.* **607**, 1–10 (2014).
27. Srinivasan, N. et al. Plastic deformation and corrosion in austenitic stainless steel: a novel approach through microtexture and infrared spectroscopy. *Corros. Sci.* **111**, 404–413 (2016).
28. Kamachi Mudali, U. et al. On the pitting corrosion resistance of nitrogen alloyed cold worked austenitic stainless steels. *Corros. Sci* **44**, 2183–2198 (2002).
29. Li, Y. Z., Wang, X. & Zhang, G. A. Corrosion behaviour of 13Cr stainless steel under stress and crevice in 3.5 wt.% NaCl solution. *Corros. Sci.* **163**, 108290 (2020).
30. Lv, J., Guo, W. & Liang, T. The effect of pre-deformation on corrosion resistance of the passive film formed on 2205 duplex stainless steel. *J. Alloys Compd.* **686**, 176–183 (2016).
31. Lebrini, M. et al. Corrosion protection of galvanized steel and electroplating steel by decanoïc acid in aqueous solution: Electrochemical impedance spectroscopy, XPS and ATR-FTIR. *Corros. Sci.* **51**, 1201–1206 (2009).
32. Jorcin, J. B., Orazem, M. E., Pébère, N. & Tribollet, B. CPE analysis by local electrochemical impedance spectroscopy. *Electrochim. Acta* **51**, 1473–1479 (2006).
33. Ramya, S., Nanda Gopala Krishna, D. & Kamachi Mudali, U. In-situ Raman and X-ray photoelectron spectroscopic studies on the pitting corrosion of modified 9Cr-1Mo steel in neutral chloride solution. *Appl. Surf. Sci.* **428**, 1106–1118 (2018).
34. Wang, S. et al. In-situ quantification and density functional theory elucidation of phase transformation in carbon steel during quenching and partitioning. *Acta Mater.* **221**, 117361 (2021).

35. Lee, J. S., Fushimi, K., Nakanishi, T., Hasegawa, Y. & Park, Y. S. Corrosion behaviour of ferrite and austenite phases on super duplex stainless steel in a modified green-death solution. *Corros. Sci.* **89**, 111–117 (2014).

36. Peguet, L., Malki, B. & Baroux, B. Influence of cold working on the pitting corrosion resistance of stainless steels. *Corros. Sci.* **49**, 1933–1948 (2007).

37. Ralston, K. D. & Birbilis, N. Effect of grain size on corrosion: a review. *Corrosion* **66**, 075005–075005-13 (2010).

38. Balusamy, T., Kumar, S. & Sankara Narayanan, T. S. N. Effect of surface nano-crystallization on the corrosion behaviour of AISI 409 stainless steel. *Corros. Sci.* **52**, 3826–3834 (2010).

39. Roese, P., Keutner, C., Berges, U., Espeter, P. & Westphal, C. Photoemission electron microscopy as a tool for studying steel grains. *Metall. Mater. Trans. A* **48**, 1484–1490 (2017).

40. Heijboer, W. M. et al. Redox behaviour of over-exchanged Fe/ZSM5 zeolites studied with in-situ soft X-ray absorption spectroscopy. *Phys. Chem. Chem. Phys.* **5**, 4484–4491 (2003).

41. De Groot, F. M. F. et al. 1s2p Resonant inelastic X-ray scattering of iron oxides. *J. Phys. Chem. B* **109**, 20751–20762 (2005).

42. Figueiredo, M. O. et al. Chemical study of passivating chromium oxide films by soft X-ray absorption spectroscopy. *Analyst* **119**, 609–611 (1994).

43. Yitamben, E. N. et al. Correlation between morphology, chemical environment, and ferromagnetism in the intrinsic-vacancy dilute magnetic semiconductor Cr-doped Ga_2Se_3/Si(001). *Phys. Rev. B* **83**, 045203 (2011).

44. Stavitski, E. & De Groot, F. M. F. The CTM4XAS program for EELS and XAS spectral shape analysis of transition metal L edges. *Micron* **41**, 687–694 (2010).

45. Lee, H. J. et al. Valence states and occupation sites in $(Fe,Mn)_3O_4$ spinel oxides investigated by soft x-ray absorption spectroscopy and magnetic circular dichroism. *J. Condens. Matter Phys.* **20**, 295203 (2008).

46. Wan, S. et al. Chemical nature of alkaline polyphosphate boundary film at heated rubbing surfaces. *Sci. Rep.* **6**, 26008 (2016).

47. Sarveena, S. et al. Synthesis, phase composition, Mössbauer and magnetic characterization of iron oxide nanoparticles. *Phys. Chem. Chem. Phys.* **18**, 9561–9568 (2016).

48. Suturin, S. M. et al. Tunable polymorphism of epitaxial iron oxides in the four-in-one ferroic-on-GaN system with magnetically ordered α-, γ-, ε-Fe_2O_3, and Fe_3O_4 layers. *Phys. Rev. Mater* **2**, 073403 (2018).

49. Frazer, B. H., Gilbert, B., Sonderegger, B. R. & De Stasio, G. The probing depth of total electron yield in the sub-keV range: TEY-XAS and X-PEEM. *Surf. Sci.* **537**, 161–167 (2003).

50. Tamura, H. The role of rusts in corrosion and corrosion protection of iron and steel. *Corros. Sci.* **50**, 1872–1883 (2008).

51. Nazarov, A. & Thierry, D. Application of Volta potential mapping to determine metal surface defects. *Electrochim. Acta* **52**, 7689–7696 (2007).

52. Tardio, S., Abel, M.-L., Carr, R. H., Castle, J. E. & Watts, J. F. Comparative study of the native oxide on 316L stainless steel by XPS and ToF-SIMS. *J. Vac. Sci. Technol., A* **33**, 05E122 (2015).

53. Detriche, S. et al. XPS fast depth profile of the native oxide layers on AISI 304, 316 and 430 commercial stainless steels and their evolution with time. *J. Electron Spectrosc. Relat. Phenom.* **243**, 146970 (2020).

54. Liu, C. et al. Effect of inclusions modified by rare earth elements (Ce, La) on localized marine corrosion in Q460NH weathering steel. *Corros. Sci.* **129**, 82–90 (2017).

55. Tobias, R. F. & Nobe, K. Electrochemical behavior of rotating iron disks: effect of Fe(III). *J. Electrochem. Soc.* **122**, 65–70 (1975).

56. Gomez, A., Dina, G. & Kycia, S. The high-energy x-ray diffraction and scattering beamline at the Canadian light source. *Rev. Sci. Instrum.* **89**, 063301 (2018).

57. Aksela, S. et al. Finnish beamline at MAX-laboratory: progress in the photon energy resolution. *Rev. Sci. Instrum.* **66**, 1621–1623 (1998).

58. Cao, W. et al. X-ray photoemission electron microscope determination of origins of room temperature ferromagnetism and photoluminescence in high Co-content $Co_xZn_{1-x}O$ films. *Surf. Rev. Lett.* **21**, 1450058 (2014).

59. Abbate, M. et al. Probing depth of soft x-ray absorption spectroscopy measured in total-electron-yield mode. *Surf. Interface Anal.* **18**, 65–69 (1992).

60. Hamada, E. et al. Direct imaging of native passive film on stainless steel by aberration corrected STEM. *Corros. Sci.* **52**, 3851–3854 (2010).

61. Fredriksson, W., Malmgren, S., Gustafsson, T., Gorgoi, M. & Edström, K. Full depth profile of passive films on 316L stainless steel based on high resolution HAXPES in combination with ARXPS. *Appl. Surf. Sci.* **258**, 5790–5797 (2012).

62. Marini, F. & Amigo, J. M. Unsupervised exploration of hyperspectral and multi-spectral images. *Data Handl. Sci. Technol* **32**, 93–114 (2020).

63. Dhanachandra, N., Manglem, K. & Chanu, Y. J. Image segmentation using K-means clustering algorithm and subtractive clustering algorithm. *Procedia Comput. Sci.* **54**, 764–771 (2015).

ACKNOWLEDGEMENTS

AUTHOR CONTRIBUTIONS

H.S., E.R. and W.C. conceived the study and H.S. developed the methodology under the project initialization and funding acquisitions from Y.X., J.K. and M.H. H.S., E.R., Y.N. and A.Z. conducted X-PEEM, H.Y. and T.Z. performed electrochemical measurement, G.K. carried out HE-SXRD, H.S., E.R., S.W., M.K. and W.C. analyzed, interpreted the results, and wrote the initial manuscript, F.M.F.G. offered advice and simulated XAS concerning the interpretation of XAS results. All authors discussed the results and contributed to the final version of the manuscript.

COMPETING INTERESTS

The authors declare no competing interests.

ADDITIONAL INFORMATION

Supplementary information The online version contains supplementary material available at https://doi.org/10.1038/s41529-022-00263-z.

Correspondence and requests for materials should be addressed to Yi Xiong or Wei Cao.

Reprints and permission information is available at http://www.nature.com/reprints

Publisher's note Springer Nature remains neutral with regard to jurisdictional claims in published maps and institutional affiliations.